

Isotropic TFT Characteristics in the {100}-Oriented Grain-Boundary-Free Laser-Crystallized Si Thin Films

Nobuo Sasaki ^{1,2,*} , Satoshi Takayama ² , Rikuto Sasai ² and Yukiharu Uraoka ²¹ Sasaki Consulting, Kawasaki 212-0012, Japan² Division of Materials Science, NAIST, Ikoma 6330-0192, Japan

* Correspondence: sassasaki@yahoo.co.jp

Abstract: Isotropic TFT characteristics are realized in the {100}-oriented grain-boundary-free 60 nm thick Si film obtained by the continuous-wave laser lateral crystallization, where the grain- and sub-boundaries are defined as the crystallographic boundaries having misfit angles of $\theta > 15^\circ$ and $\theta < 15^\circ$, respectively. Sub-boundaries are observed in the film parallel to the scan directions; the misfit angles were 5–10° and the sub-boundary density was 0.02956 μm^{-1} . Sub-grains, joined by the sub-boundaries, have widths of 8 ~ 69 μm . The cumulative distributions of mobility, threshold voltage, and subthreshold swing agree well between the parallel and perpendicular TFTs in the film, where parallel or perpendicular means the source-to-drain directions to the laser scan direction. The maximum mobilities of the parallel and perpendicular TFTs are 695 and 663 cm^2/Vs , respectively. The trap-state density N_T in the sub-boundaries estimated from the product of the bond efficiency η and the dangling bond density decreases by two decades from those of the grain boundaries. A new carrier transport model of the current flow across the sub-boundary is proposed instead of the thermionic emission model for the grain boundaries.

Keywords: sub-boundary; isotropic mobility; CW laser crystallization; TFT; trap-state density



Citation: Sasaki, N.; Takayama, S.; Sasai, R.; Uraoka, Y. Isotropic TFT Characteristics in the {100}-Oriented Grain-Boundary-Free Laser-Crystallized Si Thin Films. *Crystals* **2023**, *13*, 130. <https://doi.org/10.3390/cryst13010130>

Academic Editors: Dah-Shyang Tsai and Andreas Thissen

Received: 4 December 2022

Revised: 31 December 2022

Accepted: 7 January 2023

Published: 11 January 2023



Copyright: © 2023 by the authors. Licensee MDPI, Basel, Switzerland. This article is an open access article distributed under the terms and conditions of the Creative Commons Attribution (CC BY) license (<https://creativecommons.org/licenses/by/4.0/>).

1. Introduction

As is well known, various semiconductor materials for thin-film-transistors (TFTs) have been studied, such as amorphous-Si, organic semiconductors, oxide semiconductors, laser-crystallized Si, etc., in order to realize flat panel displays (FPDs) [1], smart sensors [2] and wearable devices [3,4] on glass or flexible substrates. The mobility of the laser-crystallized TFTs is $>200 \text{ cm}^2/\text{Vs}$, and those of other TFTs are $<60 \text{ cm}^2/\text{Vs}$ [4,5]. The laser-crystallized Si TFTs have another advantage in making CMOS circuits, enabling low standby power consumption. Pulse excimer laser annealing (ELA) was developed to crystallize amorphous-Si films on SiO_2 -coated glass for application in flat panel displays (FPDs) [6,7]. Continuous-wave laser lateral crystallization (CLC) has also been developed for SiO_2 -coated glass [8–11]. ELA has been the sole commercialized technology of laser crystallization thus far. CLC has been a candidate for high-end applications, such as monolithic three-dimensional integrations, high-speed smart sensors, and systems on FPDs because thin-film-transistors (TFTs) on CLC films show a potential to realize high mobilities comparable to those of bulk field-effect transistors (FETs), even with the crystallization on insulating substrates at room temperature. However, the film obtained by the conventional CLC with the elliptic line-beam comprised grain boundaries (GBs) of a misfit angle $\theta > 15^\circ$, where randomly oriented narrow grains were observed longitudinally extending along the scan having surface orientations of both {100} and {110} in the crystallized film [9]. It is required to obtain GB-free CLC films to realize isotropic-high mobility in TFTs comparable to those of bulk FETs.

The maximum parallel TFT mobility of 925 cm^2/Vs but the low perpendicular TFT mobility of 480 cm^2/Vs were observed for the film crystallized with the six-times overlapped CLC [12], where parallel or perpendicular means the source-to-drain directions of

TFTs to the laser scan direction. The title of the paper claimed that the TFTs were fabricated on the film comprising low-angle GBs, but the EBSD picture in the paper clearly shows that this film contained GBs with $15^\circ < \theta < 180^\circ$ as well [12]. The reported small ratio of the perpendicular to parallel mobilities of 0.52 [12] suggests the existence of large-angle GBs in their film.

The remaining GBs in the conventional CLC elongated parallel to the scan direction results in anisotropy in the electrical characteristics of TFTs. The mobilities of the perpendicular TFTs were 60–70% of those of the parallel TFTs in the conventional CLC films, with GBs of $\theta > 15^\circ$ [9]. It is required to remove the GBs from the active region of the TFT in order to realize the isotropic electrical characteristics of the TFTs and to increase mobility further.

The CLC crystallization, using a micro-chevron-laser-beam [13], made narrow stripes of 5–10 μm width and a few mm in length. The surface orientation of the stripe tended to rotate continuously with the scan travel, although GBs ($5^\circ < \theta < 65^\circ$) were not detected; however, twin boundaries of $\Sigma 3$ with a θ of 60.0 or 70.5° across the stripes were frequently observed as the scan travel at a period of 50 μm [13,14]. The mobility of the parallel TFT was 548 cm^2/Vs , but the perpendicular TFT was not reported in this narrow stripe. We use the terminologies GBs and sub-boundaries (sub-Bs) [15] and define GBs as the boundaries having $\theta > 15^\circ$ and sub-Bs having $\theta < 15^\circ$, according to the generally accepted criterion of $\theta = 15^\circ$ [16].

Recently a GB-free stripe of 80–200 μm width having 99.8% {100} surface orientation within 10° has been obtained by a single scan of CLC at room temperature substrates of quartz [11,17–22] and glass [23] in air. A highly uniform line beam was scanned at an optimized laser power around the threshold of lateral growth. These films have the {100} orientations in the scan and transverse directions, as well as surface normal. These wide {100}-oriented GB-free stripes extend stably to more than 3 mm [21] or 10 mm [22] in length, so long as the scan continues. The {100} surface texture was obtained by CLC on polyimide substrates as well [24]. Selective CLC crystallization of the TFT-active area is effective in reducing energy consumption and improving the throughput of crystallization [8,18] because the TFT-active area occupies a tiny portion in the whole LSI or FPD substrate, and the remaining Si film in the whole substrate is etched off for the wiring and light-emitting cell areas.

We have observed the isotropic mobility of TFTs fabricated in GB-free films for the first time [25]. In the present paper, we describe that the effect of the remaining sub-Bs on the TFT characteristics is negligible. We characterize sub-Bs in the GB-free films and demonstrate isotropic characteristics of TFTs, including the threshold voltage and subthreshold swing of TFTs, as well as mobility. Suppressed leakage currents are also described. The trap-state density at the sub-Bs is estimated by multiplying a dangling bond efficiency by the calculated dangling bond density, which is smaller than those of GBs by two orders of magnitude. We propose a new current model across the sub-Bs, which is different from the conventional thermionic emission model.

2. Experimental

An undoped 60 nm thick a-Si film was deposited on fused quartz by using inductively-coupled plasma chemical vapor deposition (ICP-CVD) with SiH_4 at 250 °C and 6.8 Pa. Then, a 123 nm thick SiO_2 cap was deposited by ICP-CVD with tetraethoxysilane at 300 °C and 80 Pa. After the dehydrogenation annealing at 550 °C for 1 h in N_2 , the a-Si was crystallized by an unseeded single-scanned CLC with a frequency-doubled diode-pumped solid-state Nd:YVO₄ laser at a wavelength of 532 nm, keeping the substrate at room temperature in air. A highly uniform line beam was used [17–24]. The spot size was 492 μm (long axis) \times 8 μm (short axis) with a top-flat beam shape for the long axis and Gaussian for the short axis, which was generated by utilizing a diffractive optical element (DOE). The scans were performed perpendicular to the long axis at a 12 mm/s velocity. The laser power was 4.2 W for the GB-free CLC growth and 4.0 W for the grained CLC

growth. After the cap removal, the crystal quality was characterized by electron backscatter diffraction (EBSD). The EBSD was taken at 15 kV and a tilt angle of 70° using the Hitachi SU6600 scanning electron microscope (SEM) equipped with an EBSD module from EDAX.

Top-gate TFTs were fabricated, as shown in Figure 1. The channel region was undoped. The laser-crystallized Si islands were patterned by plasma etching. A 120 nm thick gate SiO_2 was deposited by ICP-CVD with tetraethoxysilane at 300°C and 80 Pa. The gate electrodes were formed by 230 nm thick Mo sputtering and photolithography. Phosphorus ions were implanted at 90 keV to a dose of $4 \times 10^{15} \text{ cm}^{-2}$ at the source and drain regions. Activation annealing was performed at 550°C for 1 h in N_2 . Contact holes were opened, and the source and drain electrodes were formed by 230 nm thick Mo sputtering and lift-off. Finally, the $\text{N}_2\text{-H}_2$ annealing was performed at 450°C for 1 h. The channel length, L , of the TFTs was $10 \mu\text{m}$, and the width, W , was $5 \mu\text{m}$. The TFT characteristics were measured with a Precision 4156C semiconductor parameter analyzer. The effective field-effect mobilities μ were derived from the following equation of the linear region assuming a uniform carrier distribution in the channel even with the sub-boundaries at a sufficiently small drain voltage, V_D , of 0.1 V.

$$I_D = \mu C_{ox} (W/L) \cdot (V_G - V_T) V_D \quad (1)$$

where I_D is the drain current, C_{ox} is the gate capacitance per unit area, V_G is the gate voltage, V_T is the threshold voltage, and V_D is the drain voltage.

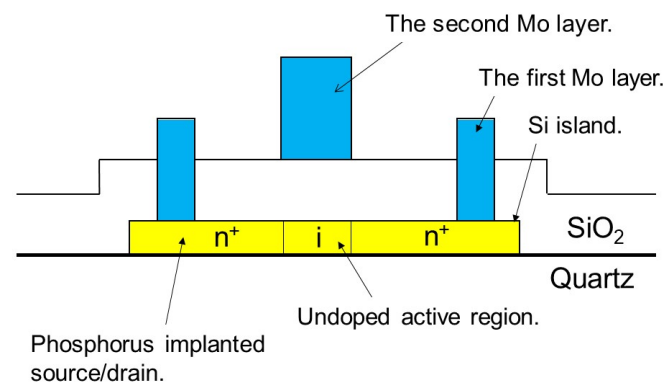


Figure 1. Schematic view of the structure of the fabricated TFT.

3. Results

3.1. The Sub-Grains (Sub-G) and Sub-Boundaries (Sub-B) in the GB-Free Area

Figure 2 shows the misfit boundaries along the laser scan of the $\{100\}$ -oriented GB-free film. Figure 2a shows the GBs with a misfit angle of $\theta > 15^\circ$. A $203 \mu\text{m}$ wide GB-free stripe was obtained along the laser scan. Figure 3 shows the GB-Free region is oriented to $\{100\}$ in all the three directions of surface normal, scan, and transverse directions simultaneously. The twin boundaries were occluded in these GB-free regions.

Figure 2b shows all the boundaries with $\theta > 2^\circ$, including both the sub-Bs and GBs. Figure 2b shows five straight sub-Bs with a θ of $5 \sim 10^\circ$ in the GB-free region running parallel to each other and the scan direction. The density of these sub-Bs is $0.02956 \text{ lines } \mu\text{m}^{-1}$. Sub-grains (sub-Gs) joined by the sub-Bs have widths of $8 \sim 69 \mu\text{m}$. A few tiny lineages with limited length and $\theta = 2 \sim 5^\circ$ are observed.

In the outside edges of the $203 \mu\text{m}$ wide $\{100\}$ -oriented GB-free region, two grained CLC stripes of 118 or $149 \mu\text{m}$ in width were observed. The EBSD Inverse Pole Figure (IPF) analysis showed that these side regions also have a $\{100\}$ orientation in the surface normal direction but comprised many grains with different in-plane orientations of $\{100\}$, $\{310\}$, $\{210\}$, $\{320\}$, and $\{110\}$ in the scan or transverse direction, as shown in Figure 3.

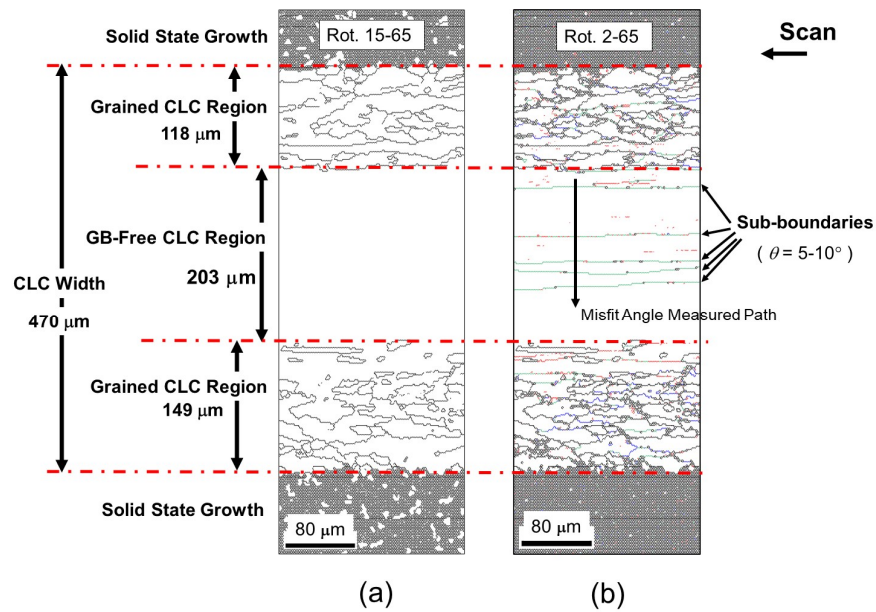


Figure 2. Crystallographic boundaries of the CLC stripe at a laser power close to the threshold of lateral grain growth. (a) Grain boundaries ($15^\circ < \theta < 65^\circ$); (b) sub-boundaries ($-$: $2^\circ < \theta < 5^\circ$, $-$: $5^\circ < \theta < 10^\circ$, and $-$: $10^\circ < \theta < 15^\circ$) and grain boundaries ($-$: $15^\circ < \theta < 65^\circ$). The path along which the misfit angle was measured is indicated by an arrow.

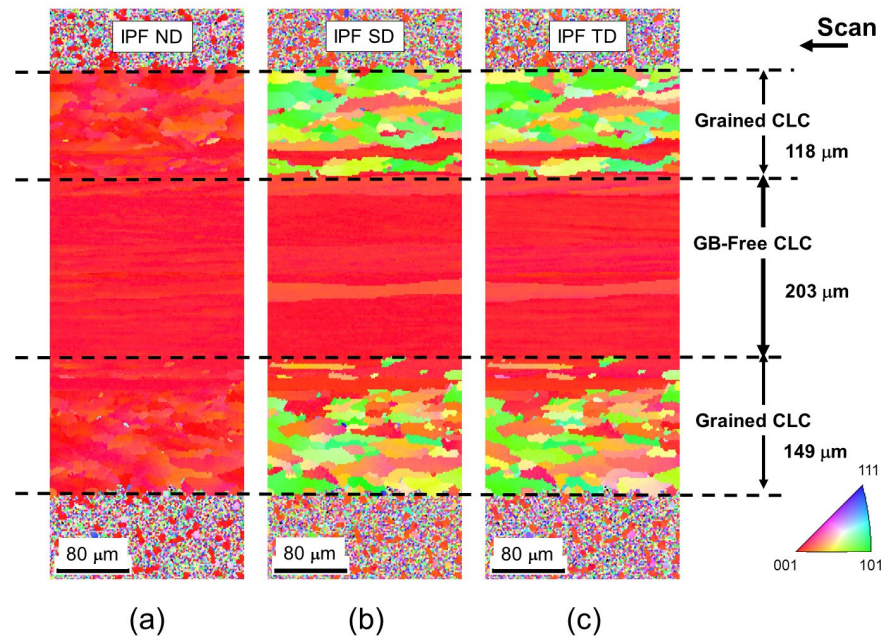


Figure 3. EBSD Inverse Pole Figure (IPF) maps of the CLC stripe at a laser power close to the threshold of lateral grain growth. (a): IPF map in the surface normal direction, (b) IPF map in the scan direction, and (c) IPF map in the transverse direction.

The sub-Bs detected in Figure 2b are tilt boundaries [15] because the surface orientation is kept uniformly at $\{100\}$, as shown in Figure 3. The $\{100\}$ orientation in the surface normal is realized by the minimum interfacial energy between Si $\{100\}$ and SiO_2 , and the $\{100\}$ in the scan direction is by the fastest growth direction of $\langle 100 \rangle$ in Si [11]. The $\{100\}$ in the transverse direction is fixed uniquely after the orientation determination of the surface normal and scan directions. The misfit angle θ profiles along the path, indicated by an arrow in Figure 2b, are shown in Figure 4. The point-to-point curve shows almost the same

absolute misfit angle θ in each sub-B, and it is obvious that the neighboring sub-Gs tilt alternately in opposite directions from the point-to-origin curve.

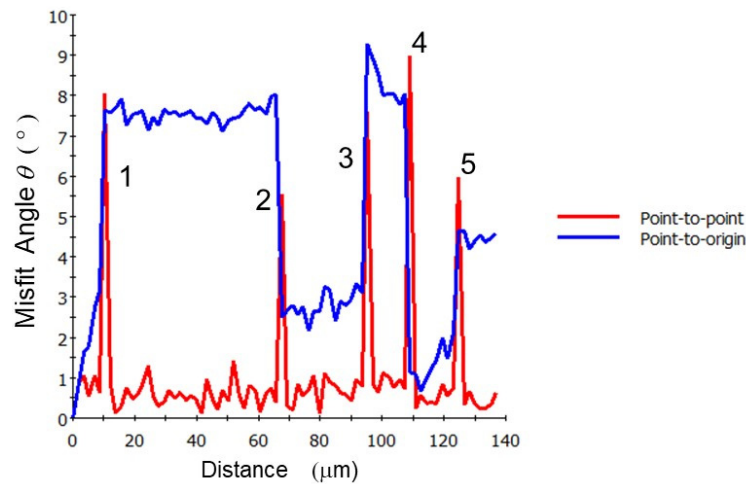


Figure 4. Misfit angle profile along the straight line drawn in Figure 3b. The red line shows the misfit between neighboring measured points, and the blue line shows the misfit of the measured point from the starting point.

For the sub-B, the crystallographic structure is described by a dislocation array [15,16] because of the small misfit angle of $\theta < 15^\circ$. We have found that there are two types of sub-Bs in the GB-free films. Figure 5 shows schematic views of the tilt boundaries described by the edge dislocation arrays. Figure 5a shows the dislocation arrays in the GB-free film. Neighboring sub-Bs are formed by dislocations with opposite polarities to each other with the same (100) surface normal axis, resulting in almost the same in-plane orientations throughout the film, as shown in Figure 3b,c. If all the sub-Bs comprise dislocations with the same polarities, the orientation in the scan direction of the film bends to one direction by the dislocation arrays, as shown in Figure 5b.

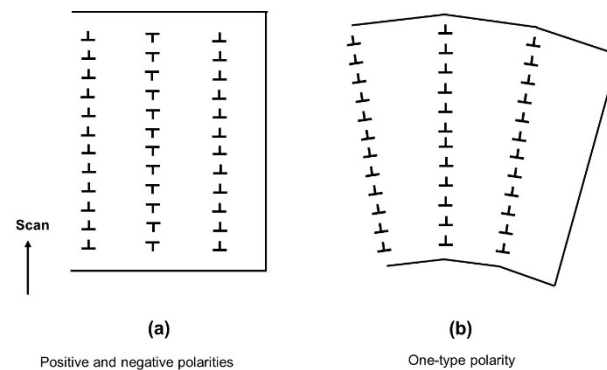
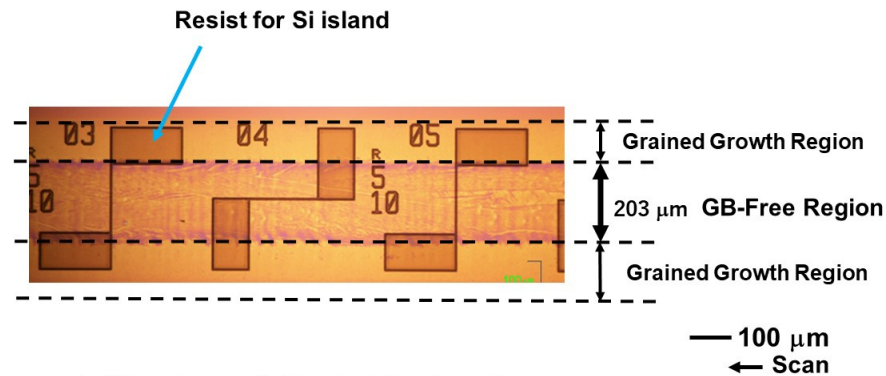


Figure 5. Schematic view of the tilt boundaries described by edge dislocation arrays. (a) configuration of tilt boundaries to keep the same in-grain crystal orientations. (b) configuration of tilt boundaries with the dislocations with the same polarities resulting in the bending of the in-grain crystal orientations.

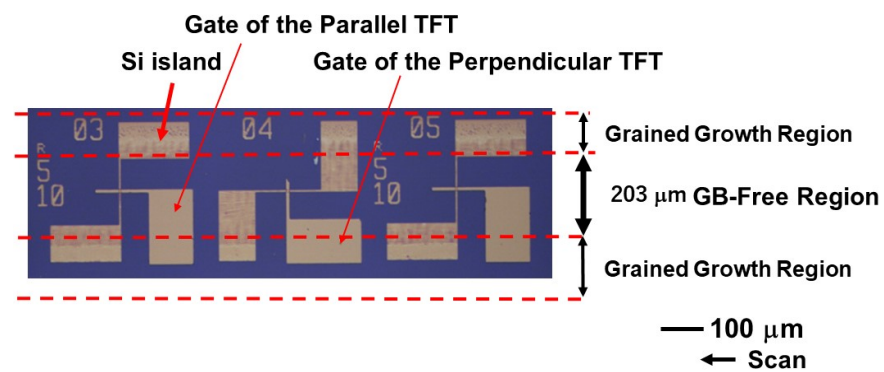
3.2. TFT Alignment in the Laser Scanned Stripe and Contact Resistance

Figure 6 shows the TFTs' alignment to the laser scan: (a) just after the island patterning and (b) after the gate patterning. The parallel and perpendicular TFTs were fabricated alternately in the same laser scan with a period of $412 \mu\text{m}$. The channel regions were placed in the GB-free stripe having a $203 \mu\text{m}$ width. The channel length and width were $10 \mu\text{m}$ and $5 \mu\text{m}$, respectively, for both the parallel and perpendicular TFTs. The n^+ wiring and contact regions were placed inside the grained or GB-free CLC stripes with a total

470 μm width. Good contact characteristics were obtained if the contacts were formed inside the grained CLC region. The phosphorus activation was carried out by the solid-phase epitaxial growth from the bottom crystalline Si layer by the 550 $^{\circ}\text{C}$ furnace annealing; the amorphous layer is solely induced by ion implantation near the front surface of the 60 nm Si film.



(a) After Island Resist Patterning



(b) After Gate Mo Patterning

Figure 6. Optical micrograph of the TFT fabrication: (a) after the island patterning and (b) after the gate patterning. The channel length was 10 μm with a width of 5 μm for both parallel and perpendicular TFTs.

3.3. TFT Characteristics in the GB-Free CLC Region

The measured distributions of the electrical characteristics of TFTs show no difference between the parallel and perpendicular TFTs. The cumulative distributions of the obtained effective field-effect mobility, threshold voltage, and subthreshold swing agree well between the parallel and perpendicular TFTs in the GB-free films, as shown in Figure 7a–c, respectively. The remaining sub-boundaries in the {100}-oriented GB-free region did not affect the electrical characteristics of the TFTs. If the sub-boundaries did affect the electrical characteristics, the obtained cumulative TFT mobilities would differ between the parallel and perpendicular TFTs. A small SS value of 60 mV/dec around the theoretical limit at room temperature was obtained. Figure 7a gives

$$\mu_{\parallel} = \mu_{\perp} \quad (2)$$

where μ_{\parallel} and μ_{\perp} are the effective field-effect mobilities of the parallel and perpendicular TFTs, respectively.

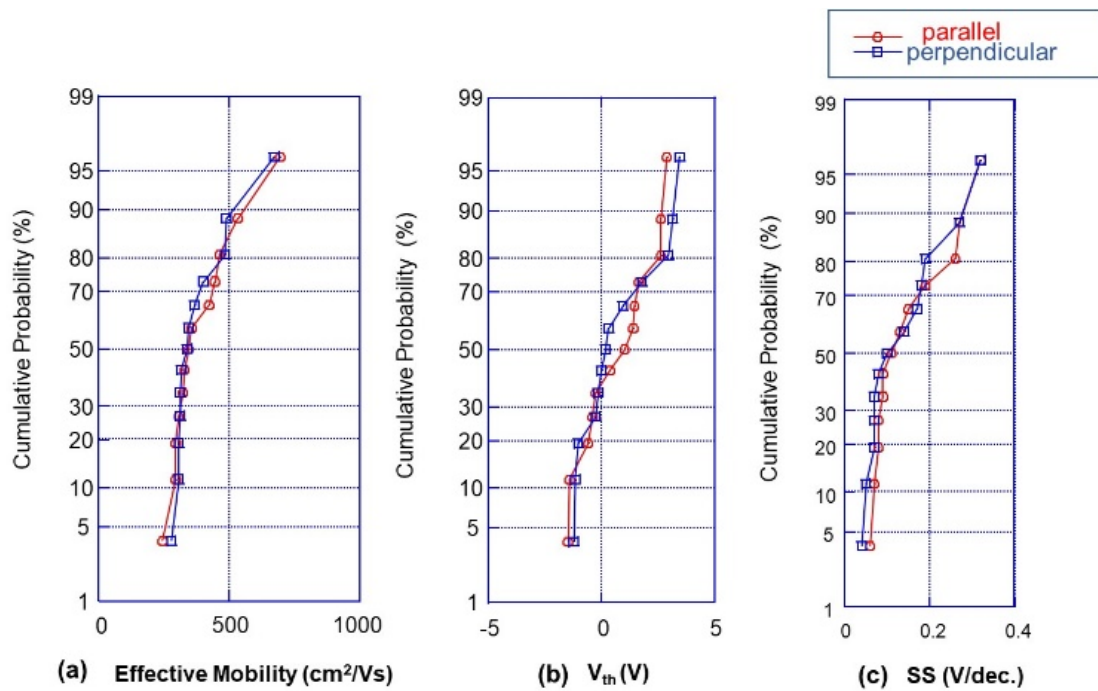


Figure 7. Cumulative distributions of electrical characteristics for the parallel and perpendicular TFTs having channel regions made in GB-free stripes. $L = 10 \mu\text{m}$, and $W = 5 \mu\text{m}$. (a) Effective field-effect mobility, (b) threshold voltage V_{th} (V), and (c) subthreshold swing SS (V/dec.).

Figure 8 shows the electrical characteristics of the parallel and perpendicular TFTs with the maximum effective mobilities. The maximum mobilities are almost the same between the parallel and perpendicular TFTs; $695 \text{ cm}^2/\text{Vs}$ was obtained for the parallel TFT, and $663 \text{ cm}^2/\text{Vs}$ was obtained for the perpendicular TFT. The steep peak observed in the $\mu-V_G$ curve is similar to the conventional MOSFETs [26–28]. The I_D-V_G curve becomes steeper when the low substrate impurity concentration becomes low following the universal curve [26,27] and when the trap-state density in the boundary becomes low [28].

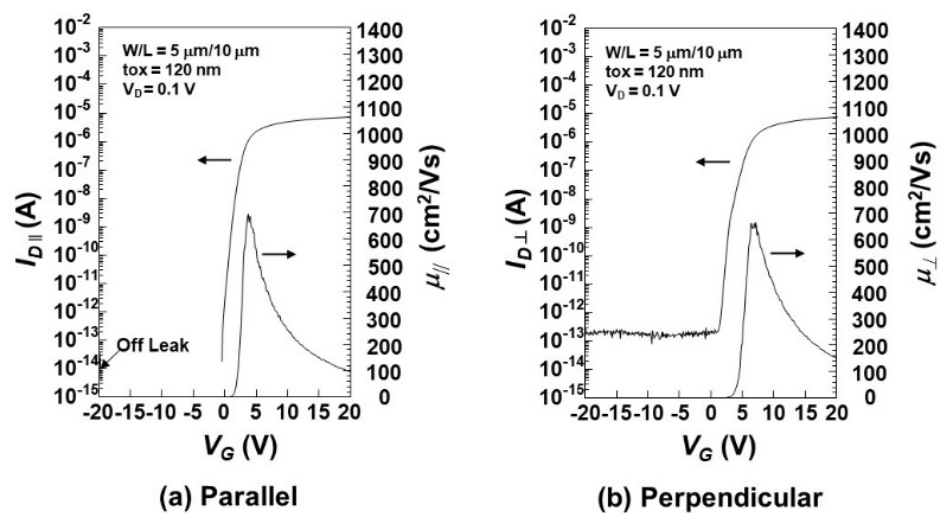


Figure 8. Drain currents I_D and effective field-effect mobilities μ as a function of the gate voltage V_G for the parallel and perpendicular TFT, respectively. (a) The parallel TFT with maximum mobility and (b) the perpendicular TFT with maximum mobility. Drain voltage V_D was 0.1 V. The maximum values of field-effect mobilities were $\mu_{||} = 695 \text{ cm}^2/\text{Vs}$ and $\mu_{\perp} = 663 \text{ cm}^2/\text{Vs}$.

Figure 9 shows the variations in the drain current I_D versus gate voltage V_G characteristics and the mobility μ versus V_G characteristics in the GB-free TFTs. The characteristics between the perpendicular and parallel TFTs show the same tendency, including variations in these characteristics. The observed TFT variations are independent of the current direction of the scan. The leakage currents of most TFTs are well suppressed below 1 fA, but some devices accidentally show a larger leakage current of 0.1 pA. The increase in the leakage current observed at a high negative gate voltage from -20 V to -15 V is due to the conventional band-to-band tunneling.

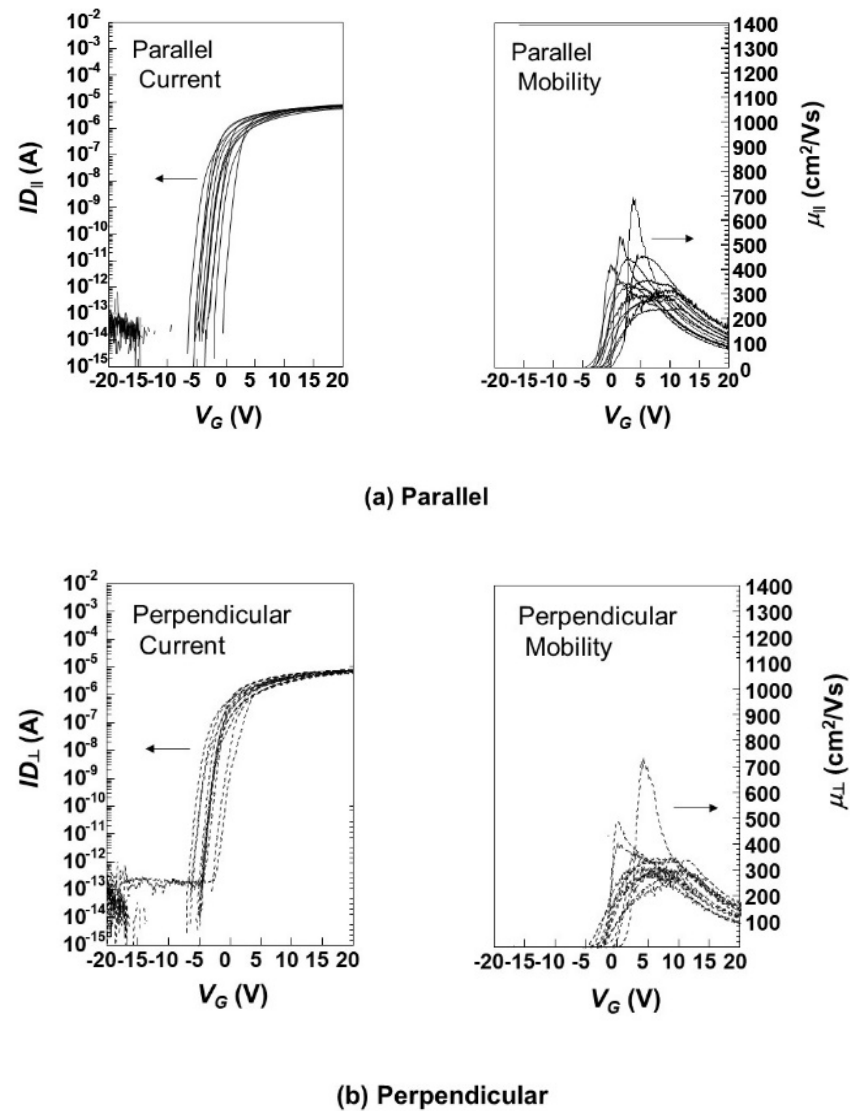


Figure 9. Variations in the characteristics of the drain currents I_D and effective mobilities μ on V_G in the measured GB-free samples: (a) the parallel TFTs and (b) the perpendicular TFTs.

Figure 10 shows the drain leakage current dependence on the drain voltage. The drain leakage current increases with the increasing drain voltage V_D . This increase shows the usual leakage current characteristics due to the band-to-band tunneling current at the drain. This tendency also confirms that the small leakage current observed at the V_D from -15 V to -5 V is not due to the current inversion. Figure 11 shows the drain current I_D versus drain voltage V_D characteristics. No anomaly is observed in these characteristics.

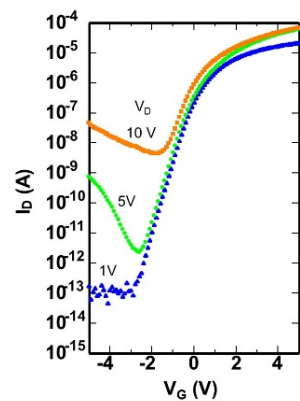


Figure 10. Drain current I_D versus gate voltage V_G characteristics as a function of the drain voltage V_D . Parallel TFT. $\mu_{\parallel} = 710 \text{ cm}^2/\text{Vs}$.

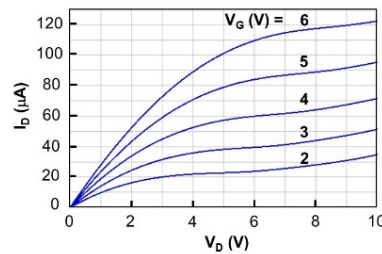


Figure 11. Drain current I_D versus drain voltage V_D characteristics as a function of the gate voltage V_G . Parallel TFT. $\mu_{\parallel} = 534 \text{ cm}^2/\text{Vs}$.

3.4. TFT Characteristic in the Grained CLC Region

Distributions of the electrical characteristics were also studied for the grained CLC film, in comparison, which was crystallized at a lower power by 0.2 W than the optimized power for GB-free crystallization. A preferential {100} surface orientation was obtained, as shown in Figure 12a. Many small grains existed, having different orientations of {100}, {310}, {210}, {320}, and {110} in the scan directions, as shown in Figure 12b. The corresponding GBs ($15^\circ < \theta$) are shown in Figure 12c, and the sub-Bs ($2^\circ < \theta < 15^\circ$) overlapped to GBs are shown in Figure 12d. The cumulative distributions of the electrical characteristics in the grained TFTs differed between the parallel and perpendicular TFTs, as shown in Figure 13.

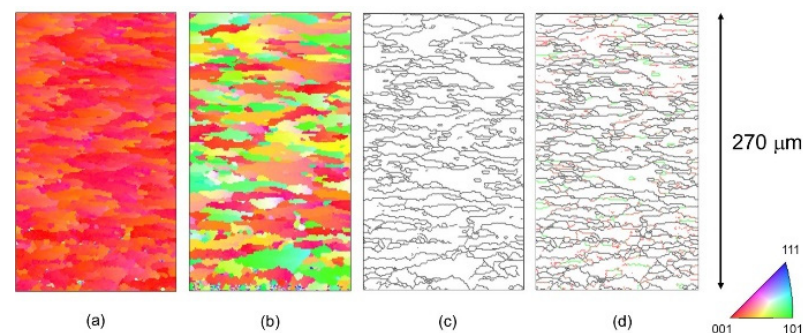


Figure 12. EBSD maps of a grained CLC film. (a) IPF-ND map, (b) IPF-SD map, (c) grain boundaries ($15^\circ < \theta < 65^\circ$), and (d) sub-boundaries ($2^\circ < \theta < 5^\circ$, $5^\circ < \theta < 10^\circ$, and $10^\circ < \theta < 15^\circ$) and grain boundaries ($15^\circ < \theta < 65^\circ$). Power was 4.0 W, and the scan velocity was 12 mm/s.

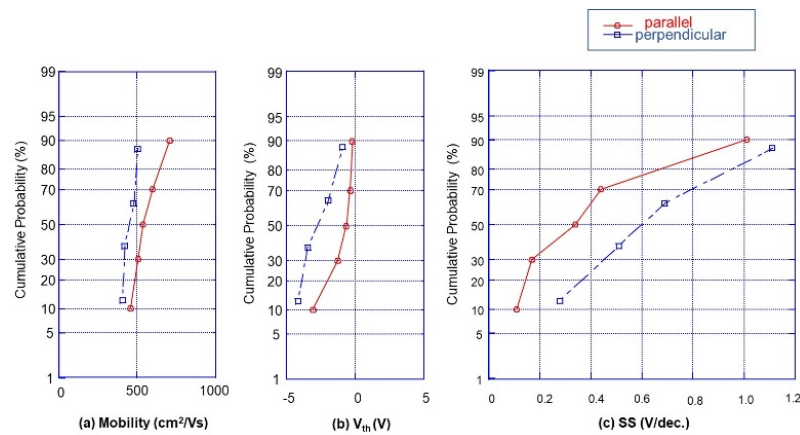


Figure 13. Cumulative distributions of the electrical characteristics in the grained CLC for the parallel and perpendicular TFTs. (a) Effective field-effect mobility, (b) threshold voltage V_{th} , and (c) subthreshold swing SS .

3.5. Comparison of Mobility Ratio Fabricated in the Present GB-Free CLC Film with Those in Other CLC Films

Figure 14 shows the ratio of the maximum effective mobilities of the perpendicular TFTs to that of the parallel TFTs. This ratio is a figure of merit for mobility isotropy. The TFTs obtained in the present GB-free films show the greatest ratio of 0.95 and a relatively large parallel mobility value of $695 \text{ cm}^2/\text{Vs}$, even with the thin 60 nm thick Si film. The highest parallel mobility was obtained by the six-times overlapped CLC on a 150 nm thick Si film [12]; however, the ratio of the TFTs was as low as 0.5 [12] due to the inferior mobility value of the perpendicular TFTs resulting from the existence of the grain boundaries and twin boundaries having a $\theta > 15^\circ$. All the conventional CLCs with a 50 nm Si thickness show a ratio of less than 0.5 [9]. The ratio and mobility in the conventional CLC generally increase with the increasing Si film thickness due to the increase in grain size, as shown in Figure 14.

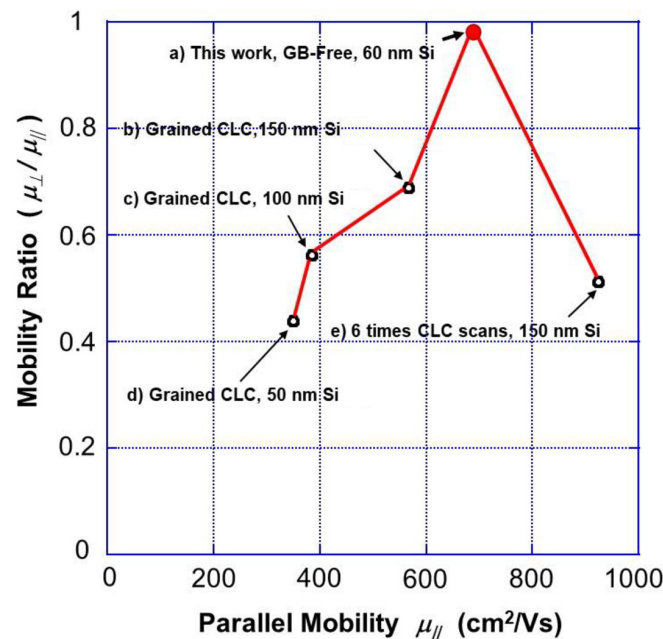


Figure 14. Ratio of the maximum mobility of the perpendicular TFTs to the parallel TFTs as a function of the maximum mobility of the parallel TFTs. The TFTs with the maximum mobility were compared in various thin-film crystallization technologies using the scanned crystallization from the melt, (a) this work, (b–d) in [9], (e) in [12].

4. Theoretical Considerations and Its Comparison with Experimental Results

4.1. Trap-State Density at the Sub-Boundaries

The tilt sub-B is described by an edge dislocation array aligned in the sub-B. The distance D between the dislocations is given by

$$D = b/(2 \sin(\theta/2)) \quad (3)$$

$$\sim b/\theta \quad (4)$$

where b is the magnitude of the Burgers vector and θ is the misfit angle of the sub-B in the radian unit [15]. The dislocation distance D in the present sub-B is 2 ~ 4 nm for $\theta = 5 \sim 10^\circ$, as shown in Figure 15. If we define the length s as a projected length of a unit cell along the dislocation line to the surface normal axis of the film, the dangling bond density per unit length is given by $2/s$, where s is equal to the lattice constant of 0.543 nm. The dangling bond density in the sub-B is calculated from D and s as

$$\text{Dangling bond density} = 2/(D \cdot s) \quad (5)$$

$$= 2\theta/(b \cdot s). \quad (6)$$

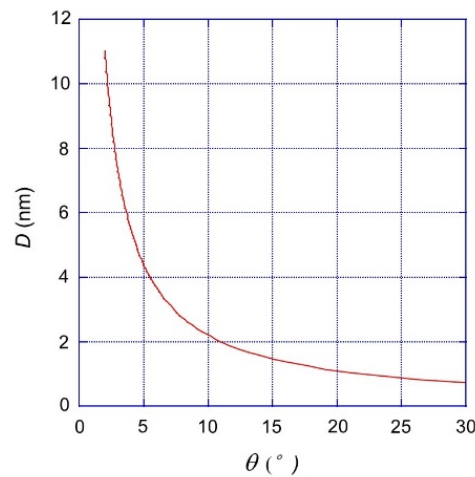


Figure 15. Dislocation distance D as a function of misfit angle θ in the boundary.

If we assume one trap is generated by one dangling bond, trap-state density N_T is given by the dangling bond density; however, this simple calculation overestimates the state density because of the bond reconstruction from the perfect dislocations and passivation of dangling bonds by hydrogen. The trap-state density N_T is given by the product of efficiency η of the dangling bond and the calculated dangling bond density as

$$N_T = \eta \times (\text{dangling bond density}). \quad (7)$$

We estimate η as 1×10^{-4} , similar to the ratio of the experimentally measured state density to the calculated dangling bond density at the Si-SiO₂ interface of the bulk MOSFETs. The interface state density Q_{ss} was measured as $6 \times 10^{10} \text{ cm}^{-2}$ for the (100) surface [29], and the number of the calculated dangling bonds is $6.8 \times 10^{14} \text{ cm}^{-2}$ for the (100) surface [30]. The N_T obtained from Equations (6) and (7) is proportional to θ , as shown in Figure 16. The effect of sub-B on the TFT characteristics decreases with the decreasing θ .

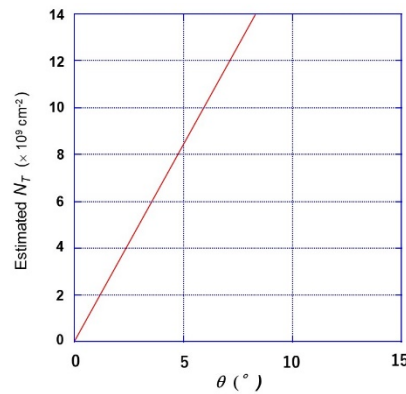


Figure 16. Trap-state density N_T estimated from dangling bond density in the sub-boundaries as a function of misfit angle θ .

4.2. Space Charge Model at the Sub-Boundaries in the Non-Doped Substrate

In the sub-G region without sub-Bs, the channel is formed by the gate-induced carriers in the undoped n-channel TFT. We assume that the free carrier is induced with the concentration n_0 of $1 \times 10^{16} \text{ cm}^{-3}$ in the inverted channel far from the sub-B, which is compatible with the generally used definition for the inversion layer. As the undoped Si substrate is floating, the electrostatic potential and the carrier concentration are uniform from the front to the back interface. From the symmetry, we treat the effect of the sub-Bs in one dimension with a vertical axis to the sub-B plane. Our model neglects the dislocation core of 0.154 nm thickness because it is very small [31]. The infinitely thin sub-B plane is assumed to have a deep trap with a density of N_T . The monoenergetic acceptor-like level is assumed and is ionized when the n-type inversion layer is formed. Due to the charged traps, two depleted regions of Δ are formed at both sides of the sub-B, resulting in a potential barrier of a height qV_B , as shown in Figure 17 [32–37], where q is the magnitude of electronic charge.

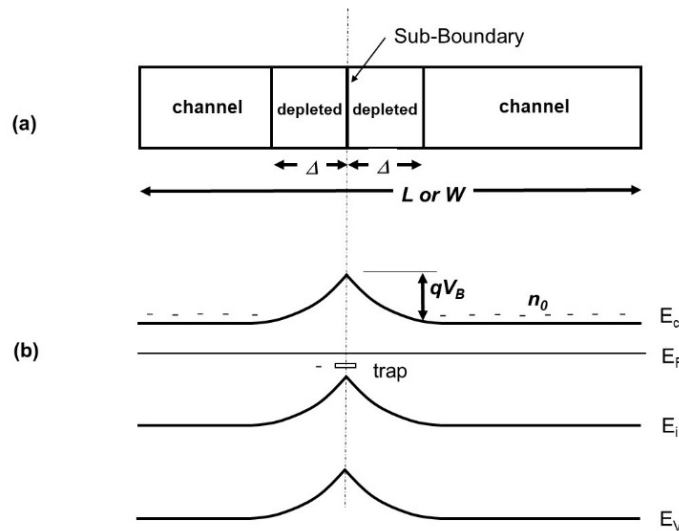


Figure 17. Theoretical model of (a) structure and (b) band diagram of the effect of sub-Bs. Δ is the width of the depleted region at each side of sub-B induced by the charged sub-B trap states. qV_B is the barrier height of free carriers in the sub-B.

The depleted region Δ is roughly estimated by the charge neutrality condition as

$$2\Delta \cdot n_0 = N_T, \tag{8}$$

and

$$\Delta = N_T / (2 n_0). \tag{9}$$

The calculation gives $\Delta = 4 \sim 8$ nm from (9) and the estimated N_T of $0.8 \sim 1.6 \times 10^{10} \text{ cm}^{-2}$ for the sub-Bs misfit angle θ of $5 \sim 10^\circ$.

Previous studies [28,33–40] of GBs in the poly-Si film assumed that the current flows over the potential barrier qV_B by the thermionic emission model. The N_T of the GBs in the previous study and the estimated N_T of the present sub-B are summarized in Table 1. The N_T of the sub-Bs with $\theta = 5 \sim 10^\circ$ drops more than two decades from that of GBs. The Δ of sub-B decreases by the same orders of magnitude from that of GBs. The depletion width of the GBs in the previous studies is very large, $\Delta \sim 1 \mu\text{m}$ from Equation (9) if we take $N_T = 2.1 \times 10^{12} \text{ cm}^{-2}$ typically.

Table 1. Comparison of trap-state density N_T and grain size between the GBs in the previous studies and the sub-Bs in the present work.

Data Source From	N_T (cm^{-2})	Grain Size (nm)
Seto, 1975 [33]	3.41×10^{12}	23
Baccarani et al., 1978 [34]	3.80×10^{12}	30
Lu et al., 1981 [35]	2.10×10^{12}	122
Martinez et al., 1981 [38]	1.2×10^{13}	1×10^5
Levinson et al., 1982 [36]	3.9×10^{11}	40
Fossum et al., 1983 [37]	1.00×10^{12}	1×10^3
Proano et al., 1989 [39]	$1.1 \sim 2.0 \times 10^{12}$	100
Yang et al., 1999 [28]	2.5×10^{12}	200
Walker et al., 2004 [40]	1.0×10^{13}	—
This Work	$0.8 \sim 1.6 \times 10^{10}$ (Sub-B)	2.03×10^5 (Perpendicular Grain Width) 3.38×10^4 (Perpendicular Sub-G Width)

4.3. Carrier Conduction in the Parallel TFTs

In the parallel TFTs containing one sub-B in the channel, the source-to-drain current flows mainly in the intra-sub-G region. Some winding current flows in the vicinity of the sub-B depleted regions, but the current at a distance from the depleted region Δ of sub-B will flow directly from the source to drain, as shown in Figure 18, in the same way as the free carriers in the inversion layer. The sub-B in the parallel TFTs reduces the effective channel width by an amount of 2Δ . Then the effective mobility of the parallel TFT with one sub-B in the active region is estimated as

$$\mu_{\parallel} = \mu_0 \cdot \{1 - (2\Delta)/W\} \quad (10)$$

where μ_0 is the intra-sub-G mobility. Then, μ_{\parallel} becomes

$$\mu_{\parallel} \sim \mu_0 \quad (11)$$

because $2\Delta \ll W$; the total sub-boundary depleted width is $2\Delta = 8 \sim 16$ nm and the channel width is $W = 5 \mu\text{m}$.

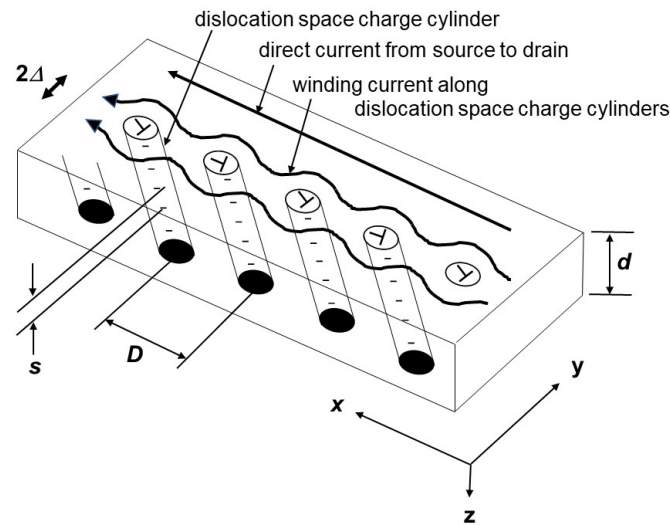


Figure 18. Model of the sub-B structure and the current in the parallel TFT.

4.4. Carrier Conduction in the Perpendicular TFTs

When a TFT active region contains one sub-B, the effective resistance R_{\perp} of the perpendicular TFTs between the source and drain is given by the series resistance of the channel resistance with a length of $(L - 2\Delta)$ and the sub-B resistance R_B

$$R_{\perp} = R_0 \cdot (1 - 2\Delta/L) + R_B \quad (12)$$

in the same way as the previous work [27–29], and the intra sub-G resistance R_0 is given by

$$R_0 = L / (W \cdot n_0 \cdot \mu_0 \cdot d) \quad (13)$$

where d is the Si film thickness, and R_B is the sub-B resistance with a length of 2Δ . On the other hand, the effective resistance R_{\parallel} of the parallel TFT is given by

$$R_{\parallel} = R_0 / (1 - 2\Delta/W). \quad (14)$$

From the experimentally obtained isotropic effective mobility given by Equation (2),

$$R_{\perp} = R_{\parallel}. \quad (15)$$

Then, as $\Delta \ll L$, (12) and (14) become

$$R_{\perp} = R_0 + R_B \quad (16)$$

and

$$R_{\parallel} = R_0. \quad (17)$$

By combining Equations (15)–(17)

$$R_B = 0. \quad (18)$$

The previous works analyzed the current across the GBs with the thermionic emission model of electrons over the barrier qV_G produced by the charged traps [28,33–40]. However, the thermionic emission model cannot explain Equation (18) because the resistance of sub-B does not vanish, even for the barrier height $qV_B = 0$. The model is invalid for the small barrier height qV_B corresponding to the small N_T of the sub-B because the model was originally derived under the assumption that

$$qV_B > kT \quad (19)$$

where kT is 2.6×10^{-2} eV at room temperature [37]. The barrier height qV_B is given by

$$qV_B = (q^2 \cdot N_T^2) / (8 \cdot \epsilon_s \cdot n_0) \quad (20)$$

for the GBs [37], where ϵ_s is the permittivity of Si. The barrier height calculated from (20) and the N_T value of the sub-Bs in the present study (shown in Table 1) is a very small value of $qV_B = 1.28 \sim 5.2 \times 10^{-4}$ eV.

In the measured 13 perpendicular TFTs, a single sub-B comprises at least one TFT. The probability is very high: $P = 0.9895$, which is calculated from the $10 \mu\text{m}$ channel length and the density of sub-Bs per unit length of $0.02956 \mu\text{m}^{-1}$ obtained from Figure 2b.

4.5. A New Model of the Perpendicular Carrier Conduction at the Sub-B

The sub-B is no more treated as a potential barrier, such as a wall, but is treated as a column of space charge cylinders allowing the current to flow between the dislocation space charge cylinders, as shown in Figure 19. The space charge cylinders are partly overlapped. The radius r of the space charge cylinder of a single dislocation is roughly estimated by the charge neutrality condition as follows:

$$2 \eta \cdot d / s = \pi r^2 \cdot d \cdot n_0. \quad (21)$$

The estimated r is 3.36 nm. This is comparable to the distance D of the dislocations in sub-B; $D = 2 \sim 4$ nm for $\theta = 5 \sim 10^\circ$, as shown in Figure 15. The carriers can go through the sub-B between the cylinders without the necessity of a high carrier energy surmounting a potential barrier. The dislocation space charge cylinders affect the negligible effect on the current, as concluded in (18), due to only one row of space charge cylinders existing vertically to the current from the source to the drain.

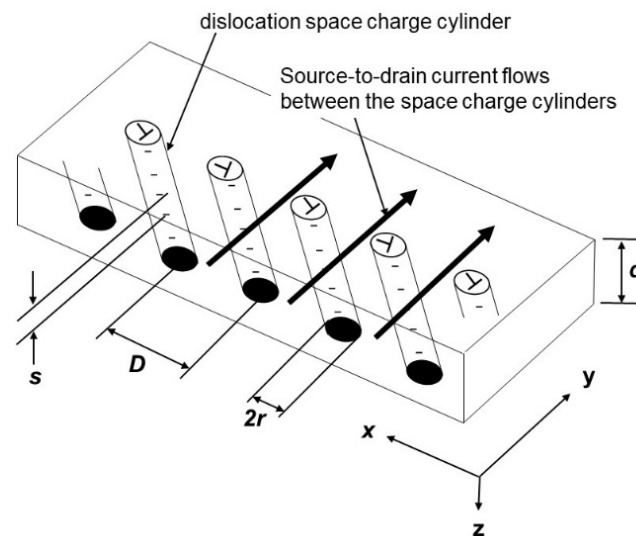


Figure 19. A new model of the current flow across a sub-B between dislocation space charge cylinders in the perpendicular TFT.

4.6. Origin of the Variations in Electrical Characteristics

The variations in electrical characteristics shown in Figure 9 are caused by some mechanisms independent of the sub-boundary direction because the distributions of parallel and perpendicular TFTs agree well. Figure 20 shows the correlation between the effective mobility and threshold voltage V_{th} . The measured points in Figure 20 gather around two clusters: in each cluster, there is no relation between parallel (red circle) and perpendicular (blue square) TFTs. In one cluster, the mobility decreases with the negative shift of V_{th} . This cluster suggests the mobility reduction due to the scattering by the charged Si-SiO₂ interface states at the front or back interface since the negative shift in V_{th} means an increase

in the interface states density Q_{ss} . The other cluster shows that the mobility is fixed at a low value, independent of V_{th} . This suggests that the mobility in this cluster is affected by the neutral scattering centers [41], such as surface roughness, and the effect of the neutral scattering center shields the effect of the Q_{ss} fluctuations. The fluctuation of Q_{ss} will be suppressed by the optimization of the gate insulator fabrication process at the low temperature of 300 °C. The surface roughness will be suppressed by optimizing the cap structure during the crystallization.

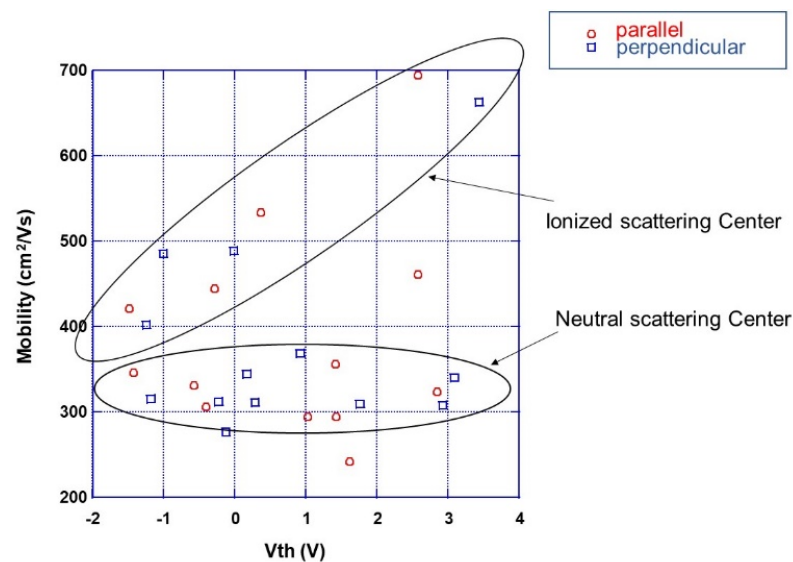


Figure 20. Correlation between measured effective mobility and threshold voltage for parallel TFTs (red circle) and perpendicular TFTs (blue square).

5. Conclusions

Isotropic TFT characteristics have been realized in the {100}-oriented grain-boundary (GB)-free Si thin films crystallized by continuous-wave laser lateral crystallization (CLC). The GB-free films comprise sub-boundaries (sub-Bs) with a misfit angle θ of 5 ~ 10°. The sub-Bs in the GB-free film extend parallel to the scan direction. The neighboring sub-grains (sub-Gs) joined by the sub-Bs tilt alternately to opposite directions, resulting in the uniform {100} in-plane orientation in the scan and transverse directions of the GB-free film. The density of the sub-Bs is 0.022956 μm^{-1} . The width of the sub-grains is 8 ~ 69 μm . The estimated trap-state density N_T of the sub-B is 0.8 ~ 1.6 $\times 10^{10}$ cm^{-2} , which drops more than two decades from that of GB. The remaining sub-B does not change the electrical characteristics of either the parallel or perpendicular TFTs. The cumulative distributions of the mobility, V_{th} , and SS are overlapped precisely between the parallel and perpendicular TFTs. A new current model across the sub-Bs has been proposed instead of the thermionic emission model of the GBs to explain the negligible impedance across the sub-B.

Author Contributions: Conceptualization, methodology, analysis, and writing, N.S.; investigation, S.T. and R.S.; resources, Y.U.; All authors have read and agreed to the published version of the manuscript.

Funding: This research received no external funding.

Data Availability Statement: No extra data is available.

Conflicts of Interest: The authors declare no conflict of interest.

References

1. Cunningham, K.L. A process for using oxide TFTs over LTPS TFTs for OLED-TV manufacturing. *Inf. Disp.* **2015**, *31*, 28–32. [[CrossRef](#)]
2. Avila-Avendano, C.; Solís-Cisneros, H.L.; Conde, J.; Sevilla-Camacho, P.A.; Quevedo-L, M.A. Modeling and SPICE simulation of the CdS/CDTe neutron detectors integrated with Si-Poly TFTs Amplifier. *IEEE Trans. Nucl. Sci.* **2022**, *69*, 1310–1315. [[CrossRef](#)]
3. Bahubalindrani, P.G.; Martins, J.; Santa, A.; Tavares, V.; Martins, R.; Fortunato, E.; Barquinha, P. High-gain transimpedance amplifier for flexible radiation dosimetry using InGaZnO TFTs. *J. Electron Devices Soc.* **2018**, *6*, 760–765. [[CrossRef](#)]
4. Facchetti, A.; Hsiao, C.-C.; Huitema, E.; Inagaki, P. Enabling wearable and other novel applications through flexible TFTs. *Inf. Disp.* **2016**, *32*, 6–11. [[CrossRef](#)]
5. Wager, J.F. Oxide TFTs: A progress report. *Inf. Disp.* **2016**, *32*, 16–21. [[CrossRef](#)]
6. Brotherton, S.D.; McCulloch, D.; Clegg, J.; Gowers, J. Excimer-laser-annealed poly-Si thin-film transistors. *IEEE Trans. Electron Devices* **1993**, *40*, 407–413. [[CrossRef](#)]
7. Mishima, Y.; Yoshino, K.; Takeuchi, F.; Ohgata, K.; Takei, M.; Sasaki, N. High-performance CMOS circuits fabricated by excimer-laser-annealed poly-Si TFTs on glass substrates. *IEEE Elec. Dev. Lett.* **2001**, *22*, 89–91. [[CrossRef](#)]
8. Sasaki, N.; Hara, A.; Takeuchi, F.; Mishima, Y.; Kakehi, T.; Yoshino, K.; Takei, M. High throughput CW-laser lateral crystallization for low-temperature poly-Si TFTs and fabrication of 16 bit SRAMs and 270 MHz shift registers. *SID Int. Symp. Dig. Tech. Pap.* **2002**, *33*, 154–157. [[CrossRef](#)]
9. Hara, A.; Takei, M.; Takeuchi, F.; Suga, K.; Yoshino, K.; Chida, M.; Kakehi, T.; Ebiko, Y.; Sano, Y.; Sasaki, N. High performance low temperature polycrystalline silicon thin film transistors on non-alkaline glass produced using diode pumped solid state continuous wave laser lateral crystallization. *Jpn. J. Appl. Phys.* **2004**, *43*, 1269–1276. [[CrossRef](#)]
10. Park, M.; Vangelatos, Z.; Rho, Y.; Park, H.K.; Jang, J.; Grigoropoulos, C. Comprehensive analysis of blue diode laser-annealing of amorphous silicon films. *Thin Solid Films* **2020**, *696*, 137779. [[CrossRef](#)]
11. Sasaki, N.; Arif, M.; Uraoka, Y.; Gotoh, J.; Sugimoto, S. Unseeded crystal growth of (100)-oriented grain-boundary-free Si thin-film by a single scan of the CW-laser lateral crystallization of a-Si on Insulator. *Crystals* **2020**, *10*, 405. [[CrossRef](#)]
12. Nguyen, T.T.; Kuroki, S.-I. Dependence of thin film transistor characteristics on low-angle grain boundaries of (100)-oriented polycrystalline silicon thin films. *Jpn. J. Appl. Phys.* **2019**, *58*, SBBJ08. [[CrossRef](#)]
13. Yeh, W.; Shirakawa, T.; Pham, A.H.; Morito, S. Twin formation in micro-chevron laser beam scanning induced one directional crystal growth in Si film on SiO₂. *Jpn. J. Appl. Phys.* **2020**, *59*, SGGJ05. [[CrossRef](#)]
14. Yeh, W.; Hirasue, M.; Ohtoge, K.; Tsuchiya, T. High performance thin-film transistors fabricated on a single crystal Si strip by micro-chevron laser beam scanning method. *Jpn. J. Appl. Phys.* **2020**, *59*, 071008. [[CrossRef](#)]
15. Andersen, P.M.; Hirth, J.P.; Lothe, J. Grain boundaries and interfaces. In *Theory of Dislocations*, 3rd ed.; Cambridge Univ. Press: Cambridge, UK, 2017; pp. 536–540.
16. Brandon, D.G. The structure of high-angle grain boundaries. *Acta Metall.* **1966**, *14*, 1479–1484. [[CrossRef](#)]
17. Sasaki, N.; Nieda, Y.; Hishitani, D.; Uraoka, Y. Power dependence of orientation in low-temperature poly-Si lateral grains crystallized by a continuous-wave laser scan. *Thin Solid Films* **2017**, *631*, 112–117. [[CrossRef](#)]
18. Sasaki, N.; Arif, M.; Uraoka, Y. Folded pixel circuit design in grain-boundary free (100) oriented LTPS stripes fabricated by selective CW-laser lateral crystallization. *SID Int. Symp. Dig. Tech. Pap.* **2018**, *49*, 755–758. [[CrossRef](#)]
19. Sasaki, N.; Arif, M.; Uraoka, Y. Transition mechanism of the thin Si-films obtained by the CW laser lateral crystallization from the grain-boundary free highly {100} oriented crystal to the twinned {211} crystal depending on the laser power. *Jpn. J. Appl. Phys.* **2019**, *58*, SBBJ02. [[CrossRef](#)]
20. Sasaki, N.; Arif, M.; Uraoka, Y. Effect of surface tension on crystal growth of Si thin films by a continuous-wave laser lateral crystallization. *Appl. Phys. Express* **2019**, *12*, 055508. [[CrossRef](#)]
21. Arif, M.; Sasaki, N.; Ishikawa, Y.; Uraoka, Y. Extension of the {100}-oriented grain-boundary free Si thin film grown by a continuous-wave laser lateral crystallization. *Thin Solid Films* **2020**, *708*, 138127. [[CrossRef](#)]
22. Arif, M.; Sasaki, N.; Takayama, S.; Uraoka, Y. Extension of a 10 mm long {100}-oriented grain boundary free silicon domain crystallized by continuous wave green laser. In Proceedings of the 21st International Meeting on Information Display, Virtual, 25–27 August 2021.
23. Sasaki, N.; Arif, M.; Uraoka, Y.; Gotoh, J.; Sugimoto, S. Crystal growth study of the grain-boundary free (100) textured Si thin films by using the CW-laser lateral crystallization. In Proceedings of the IEEE SOI-3D-Subthreshold Microelectronics Technology Unified (S3S) Conference, San Jose, CA, USA, 14–17 October 2019. [[CrossRef](#)]
24. Sasaki, N.; Arif, M.; Uraoka, Y.; Gotoh, J.; Sugimoto, S. Continuous-wave laser lateral crystallization of a-Si thin films on polyimide using a heatsink layer embedded in the buffer SiO₂. *J. Electron. Mat.* **2021**, *50*, 2974–2980. [[CrossRef](#)]
25. Sasaki, N.; Arif, M.; Takayama, S.; Gotoh, J.; Sugimoto, S.; Uraoka, Y. Isotropic TFT mobility in the (100)-oriented grain-boundary-free huge Si thin film grown by the continuous-wave-laser lateral crystallization. In Proceedings of the 2021 International Conference on Solid State Devices and Materials, Virtual, 6–9 September 2021.
26. Sodini, C.G.; Ekstedt, T.W.; Moll, J.L. Charge accumulation and mobility in thin dielectric MOS transistors. *Solid-St. Electron.* **1982**, *25*, 833. [[CrossRef](#)]
27. Chen, K.; Wann, H.C.; Dunster, J.; Ko, P.K.; Hu, C.; Yoshida, M. MOSFET carrier mobility model based on gate oxide thickness, threshold and gate voltages. *Solid-St. Electron.* **1996**, *39*, 1515. [[CrossRef](#)]

28. Yang, G.-Y.; Hur, S.-H. A physical-based analytical turn-on model of polysilicon thin-film transistors for circuit simulation. *IEEE Trans. Electron Devices* **1999**, *46*, 165. [[CrossRef](#)]
29. Sasaki, N. Change of Si-SiO₂ Interface Charge by BT Treatment. *Jpn. J. Appl. Phys.* **1973**, *12*, 1458–1459. [[CrossRef](#)]
30. Sze, S.M. Crystal Orientation Effect. In *Physics of Semiconductor Devices*; Wiley: New York, NY, USA, 1969; pp. 471–473.
31. Andersen, P.M.; Hirth, J.P.; Lothe, J. Core energy. In *Theory of Dislocations*, 3rd ed.; Cambridge Univ. Press: Cambridge, UK, 2017; pp. 203–207.
32. Mataré, H.F. Basic electrical properties of dislocations in semiconductors. In *Defect Electronics in Semiconductors*; Wiley: New York, NY, USA, 1971; pp. 145–172.
33. Seto, J.Y. The Electrical Properties of Polycrystalline Silicon Films. *J. Appl. Phys.* **1975**, *46*, 5247–5254. [[CrossRef](#)]
34. Baccarani, G.; Riccò, B.; Spadini, G. Transport properties of polycrystalline silicon films. *J. Appl. Phys.* **1978**, *49*, 5565–5570. [[CrossRef](#)]
35. Lu, N.C.-C.; Gerzberg, L.; Lu, C.-Y.; Meindl, J.D. Modeling and Optimization of Monolithic Polycrystalline Silicon Resistors. *IEEE Trans. Electron Devices*, 1981; ED-28, 818–830. [[CrossRef](#)]
36. Levinson, J.; Shepherd, F.R.; Scanlon, P.J.; Westwood, W.D.; Este, G.; Rider, M. Conductivity behavior in Polycrystalline Semiconductor Thin Film Transistors. *J. Appl. Phys.* **1982**, *53*, 1193–1202. [[CrossRef](#)]
37. Fossum, J.G.; Oritz-Conde, A. Effects of grain boundaries on the channel conductance of SOI MOSFET's. *IEEE Trans. Electron Devices* **1983**, *ED-30*, 933–940. [[CrossRef](#)]
38. Martinez, J.; Criado, A.; Piqueras, J. Grain boundary potential determination in polycrystalline silicon by the scanning light spot technique. *J. Appl. Phys.* **1981**, *52*, 1301. [[CrossRef](#)]
39. Proano, R.E.; Ast, D. Effects of the presence/absence of HCl during gate oxidation on the electrical and structural properties of polycrystalline silicon thin-film transistors. *J. Appl. Phys.* **1989**, *66*, 2189. [[CrossRef](#)]
40. Walker, P.M.; Mizuta, H.; Uno, S.; Furuta, Y.; Hasko, D.G. Improved off-current and subthreshold slope in aggressively scaled poly-Si TFTs with a single grain boundary in the channel. *IEEE Trans. Electron Devices* **2004**, *51*, 212. [[CrossRef](#)]
41. Takagi, S.; Toriumi, A.; Iwase, M.; Tango, H. On the universality of inversion layer mobility in Si MOSFET's: Part I-effects of substrate impurity concentration. *IEEE Trans. Electron. Devices* **1994**, *41*, 2357–2362. [[CrossRef](#)]

Disclaimer/Publisher's Note: The statements, opinions and data contained in all publications are solely those of the individual author(s) and contributor(s) and not of MDPI and/or the editor(s). MDPI and/or the editor(s) disclaim responsibility for any injury to people or property resulting from any ideas, methods, instructions or products referred to in the content.